An Innovative Testing Protocol to Study Spent Nuclear Fuel Vibration Integrity under Normal Condition of Transportation*

J.-A. Wang[1], H. Wang[1], H. Jiang[1], B. Bevard[2]

[1]Materials Science and Technology Division, [2]Reactor & Nuclear Systems Division
Oak Ridge National Laboratory, 1 Bethel Valley Road, Oak Ridge, Tennessee, USA

ABSTRACT

The Oak Ridge National Laboratory (ORNL) has developed the cyclic integrated reversible-bending fatigue tester (CIRFT) approach to successfully demonstrate the controllable fatigue fracture of high burnup (HBU) spent nuclear fuel (SNF) in a normal vibration mode. CIRFT enables examination of the underlying mechanisms of SNF system dynamic performance. Due to the inhomogeneous composite structure of the SNF system, the detailed mechanisms of pellet-pellet and pellet-clad interactions and the stress concentration effects at the pellet-pellet interface cannot be readily obtained from a CIRFT system measurement. Therefore, finite element analyses (FEAs) are being used to complement the experimental work by estimating values of local stresses and strains from the measured global moment-curvature. These results and their implications will be used for further investigation.

Major findings of CIRFT on the HBU SNF are as follows:
- The degree of bonding between pellets, as well as the bonding between pellets and clad in the SNF system plays an important role in the vibration performance of SNF.
- Fuel structure contributes to SNF system stiffness.
- There are significant variations in stress and curvature of SNF systems during vibration cycles resulting from segment pellet and clad interactions.
- SNF failure initiates at the pellet-pellet interface region and appears to be spontaneous.

INTRODUCTION

In the United States, spent nuclear fuel (SNF) is expected to be transported to at least one storage facility before permanent disposal. During transportation, transportation casks will experience cycling forces due to normal conditions of transport (NCT). These forces will be transmitted to the contents of the casks and SNF assemblies, resulting in localized stresses. Nuclear fuel is now regularly irradiated to high-burnup (HBU) values (>45 GWd/MTU). The presence of hydride phases in the cladding and variability in material properties could further influence fuel performance during transportation [1–2].

For these reasons, the conditions of fuel failure during NCT are being investigated. The ORNL CIRFT has been used to investigate the bending stiffness and fatigue life of HBU fuel during simulated transportation conditions [3–10]. The testing was designed to evaluate the fuel rod as a system, including the presence of fuel pellets and any fuel/clad bonding effects. The objective of this project is to develop information to support the evaluation of vibration fatigue for cask license reviews.

Testing was conducted on HBU SNF from a pressurized-water reactor (PWR) that used Zircaloy-4 (Zry-4) or M5$^{\text{TM}}$ cladding. The static tests defined the elastic and plastic responses of the fuel rod system, and the dynamic tests defined the fatigue life of the fuel rod system under constant loads. The effects of cyclic loading over a wide range of loading amplitudes were tested and evaluated to develop an understanding of the fatigue life of HBU fuel. Graphs of equivalent strain versus the number of cycles to failure (ε-N) or curvature versus the number of cycles to failure (κ-N) were developed to estimate the influence of the imposed bending on the fatigue strength. The impacts of important fuel rod phenomena such as fuel-to-clad bonding and the pellet-to-pellet pinning interaction were recognized but were not quantified. FEA

protocols were also developed to translate the global response of CIRFT examination to the local state of stress/strain and to quantify the CIRFT system biases and associated uncertainties on the HBU SNF under CIRFT [4, 11–12]. The FEA simulation results were validated and calibrated by ORNL reversal bending fatigue testing of the HBR fuel rod.

The FEA models were developed using ABAQUS. They consist of a two inch gauge section covering the Zr-4 clad and HBR pellets and interfacial layers that provide chemical cohesive bonding or mechanical radial compressive residual stresses from pellet-clad contact pressure. To estimate fuel rod system responses, including the stress profile and the associated curvature κ, bending moments (M) were applied to both ends of the fuel rod. Based on the FEA results, the flexural rigidity (EI) of the simulation cases was estimated as $EI = M/\kappa$. Three simulation cases were studied, namely, (1) section model with good interface bonding and without pellet fracture, (2) section model with perfect bond bonding at pellet-clad interfaces and debonding at pellet-pellet interfaces, and (3) section model with debonding at both pellet-clad and pellet-pellet interfaces.

The curvature of a fuel rod system estimated from global and local deflection data for the clad was studied in detail based on the tension and the compression sides of the clad. The shift of the neutral axis of the fuel composite system was investigated as a function of fatigue cycles and further validated from nonsymmetry CIRFT curvature measurement data. Based on FEA results, as well as fractured CIRFT samples that all failed at the pellet-pellet interface regions, it was found that the pellet-pellet interface regions constitute the weakest link in an SNF rod system under vibration.

CIRFT TESTING METHODOLOGY DEVELOPMENT

The objective of this project is to perform a systematic study of SNF integrity under simulated transportation conditions by using hot-cell testing technology developed recently at ORNL utilizing a CIRFT [3–10]. Currently, CIRFT testing on SNF is conducted at an ORNL hot-cell testing facility. Under Nuclear Regulatory Commission (NRC) sponsorship, ORNL completed four benchmarking tests, four static tests, and twelve dynamic or cycle tests on H. B. Robinson (HBR) high burn-up fuel. The related testing results were documented in an ORNL report (TM-2014/214); developments regarding instrumentation, test protocol, and data processing were also reported. With support from the US Department of Energy (DOE) and the NRC, testing with the CIRFT continues on HBR rods. At the same time, ORNL initiated PIE (post-irradiation examination) of selected rod segment/tested specimens and CIRFT testing on North Anna M5 and mixed oxide (MOX) SNF.

Out-of-cell study supports the ongoing ORNL hot-cell or in-cell testing. For example, the sensor benchmark refinement of the in-cell device is performed outside the cell. Although the use of CIRFT on HBR SNF rods generated a lot of significant data, a number of important issues remain to be addressed [4]. Because direct hot-cell examination in some of these issues is prohibitive due to high cost and limited access, out-of-cell study has been demonstrated to be cost effective and much more feasible when studying pre-hydride samples and prioritizing selected aging parameters. A testing system with the same configuration as that of CIRFT used in a hot cell has been developed to study the issues that emerged from hot-cell testing and also to investigate the fatigue and failure mechanisms of SNF rods that cannot be identified directly in hot-cell testing.

Effect of Probe Contact on Curvature Measurement

The CIRFT curvature measurement is based on three linear variable differential transformers (LVDTs) in direct contact with the SNF rod. Therefore, the effect of contact with the LVDT probe used for curvature measurement needs to be carefully examined under reversible bending loading. Currently the disk-shaped probe of LVDT was used in the CIRFT hot-cell testing facility.

Experimental study was performed by using two surrogate rods made of the same materials and same configuration (stainless steel tube and alumina pellets [SSAP]), and the same flat probe contact was used as seen in Figure 1b.

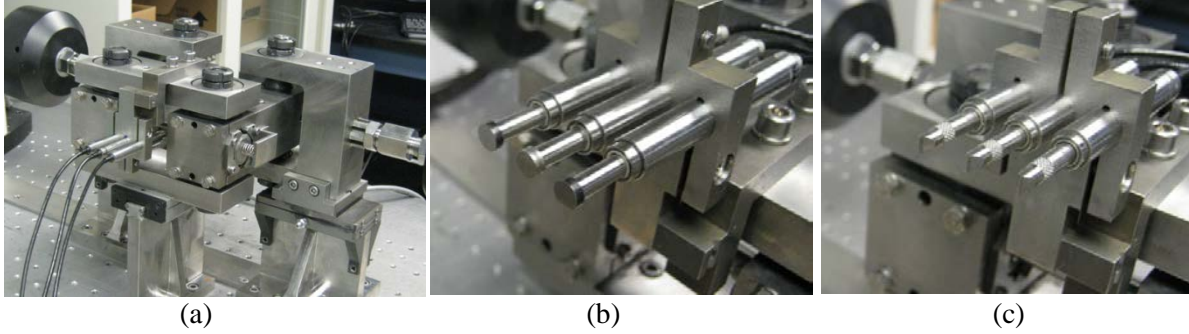(a)   (b)   (c)

Fig. 1. (a) Three curvature LVDTs being held against the rod, (b) LVDT clamp open to show flat disk probe in one configuration, and (c) chisel head probe in another configuration for benchmarking.

In order to study the effect of bending reversal on the curvature measurement, the rod was subjected to positive and negative bending. Concave and convex bending of the three LVDTs was examined. In the case of convex bending, the rod was bent toward the three LVDTs, and large-stroke LVDTs were needed thereafter. Three LVDTs with a stroke of ±5 mm were calibrated.

As shown in Fig. 2, under a similar level of applied moment, the maximum curvature obtained is significantly larger when a rod is bending concavely with respect to the LVDTs than when a rod is bending convexly. The discrepancy can be considered by adjusting sensor spacing h, as illustrated in Fig. 3. The moment-curvature curves in both cases converge if a sensor spacing adjustment Δh of 2.5 mm is used (namely, 21% of sensor spacing h and a little less than the contact radius of 3.0 mm). The actual sensor spacing adjustment can be calibrated, and the study demonstrated that the curvature based on flat-probe contact can be corrected if necessary.
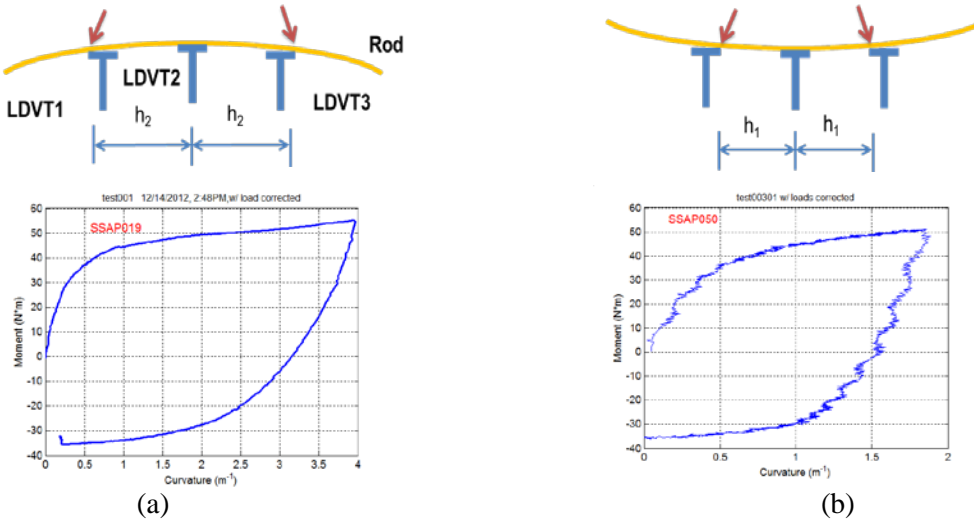

(a)   (b)

Fig. 2. Moment-curvature curves based on SSAP rod testing when the rod is bending with respect to three LVDTs (a) concavely and (b) convexly.
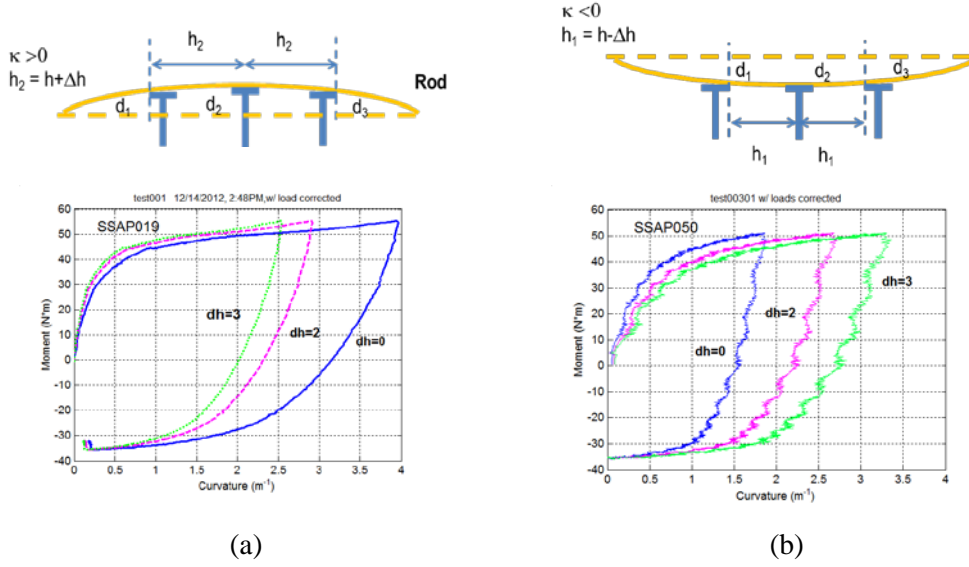
3

Fig. 3. Moment-curvature curves as a function of sensor spacing adjustment when a rod is bending with respect to three LVDTs (a) concavely and (b) convexly.

The chisel shape probe (Fig. 1c) was also used to evaluate the sensitivity of the probe shape to curvature measurements. Initial results from testing on a uniform surrogate rod indicate that the disk probe overestimates the curvature by 30% on the clad compressive side, and the disk probe underestimates the curvature by 30% on the clad tensile side. Further work is needed to using better surrogate rods with segmental fuel insert structures similar to those of SNF rods. This will help ensure a more accurate curvature adjustment factor.

Data Processing

Measurement data and online monitoring data were converted into applied moment and curvature based on the load channel output (load 1 and load 2), the loading arm (101.60 mm), and LVDT channels (LVDT 1, 2, and 3) output [4]. The moment (M) was estimated by:

$$M = F \times L \tag{1}$$

where F is the averaged value of applied loads (load 1 and load 2) from Bose dual motors, and L is the loading arm, 101.60 mm. The curvature (κ) was estimated using Eq. (2) as described below.

The curvature κ can be defined by the radius of circle as follows

$$\kappa = 1/R$$

The parameters of circle equation can be estimated based on the deflections measured by three LVDTs, d_1, d_2, d_3:

$$R = \sqrt{(x_0 - d_2)^2 + y_0^2}$$

$$x_0 = \frac{-2 m_a m_b h - m_a (d_2 + d_3) + m_b (d_1 + d_2)}{2(m_b - m_a)}$$

$$y_0 = -\frac{1}{m_a}\left(x_0 - \frac{d_1 + d_2}{2}\right) - \frac{h}{2}$$

where

$$m_a = \frac{h}{d_2 - d_1} \qquad m_b = \frac{h}{d_3 - d_2}$$

(2)

4

The equivalent strain-stress curves were obtained under the assumption that the SNF rod can be idealized as a linear elastic homogeneous material without considering the effects induced by any pellet-cladding interaction. The equivalent stress was calculated by:

$$\sigma = M \times y_{max}/I \tag{3}$$

where I is the moment of inertia, $I = I_c + I_p$, and I_c and I_p are moments of inertia of the cladding and pellet, respectively, and y_{max} is the maximum distance to the neutral axis of the test rod of the section measured by the radius of the cladding. The calculation of stress ignores the difference of elastic moduli between the cladding and the pellets, where fuel has higher stiffness. Thus, the penalty of fuel stiffness reduction applied to fuel property is intended to address the bonding deficiency at fuel and clad interface.

The equivalent strain was calculated by:

$$\varepsilon = \kappa \times y_{max}. \tag{4}$$

and the associated flexural rigidity is defined as $\Delta M/\Delta \kappa$.

Effect of Segmental Pellet Inserts of Fuel Clad to SNF Curvature Measurement

The test result of the R4 specimen is used to demonstrate the nonuniform flexural deformation observed from tests with the CIRFT under clad tension and compression cycles. Online monitoring data shown in Fig. 4 indicate a fairly flat response of flexural rigidity, with a slight drop prior to final failure under 8.89 N-m at 2.7×10^5 cycles. Figure 4b shows typical curvature measurements from SNF rod vibration testing where the clad tensile cycle shows higher curvature than that of clad compression cycle. This is primarily due to pellet-pellet-clad interactions at the triple interfacial region where two pellets and the cladding meet. At the clad compression cycle, pellet-pellet pinning can provide sufficient bending moment resistance, resulting in curvature reduction. While in a clad tension cycle, pellet-pellet pinning would no longer be available, and the clad alone will carry all the bending moment resistance. This, in addition to the stress concentration at the pellet-pellet interface region, results in a curvature increase.

(a)   (b)   (c)
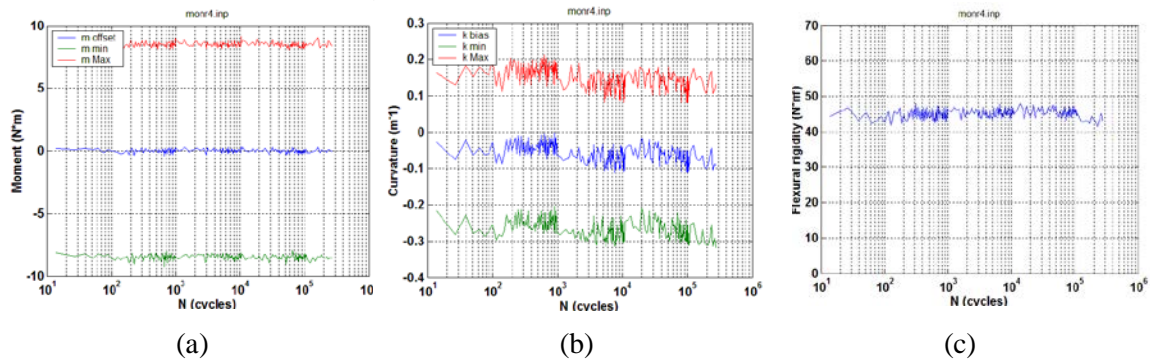
Fig. 4. Variations of (a) maximum and minimum values of moment, (b) maximum and minimum values of curvature, and (c) flexural rigidity as a function of number of cycles for specimen R4 (606B3D) (failure frequency $N_f = 2.7\times10^5$ cycles under ±8.89 N·m 5 Hz).

Mean Curvature and Maximum of Absolute Curvature Extremes

Under a load-controlling mode, the offset of the M-κ loop with respect to the κ axis can be described by the mean value of curvatures, κ_m:

$$\kappa_m = 0.5 \times (\kappa_{max} + \kappa_{min}). \tag{5}$$

5

In load-controlled cycle tests, the curvature range $\Delta\kappa = (\kappa_{max} - \kappa_{min})$ exhibited a flat response prior to failure. As a result, the rigidity was stable over most of the monitored period, followed by a slight drop prior to failure. However, the characterization of fatigue on the fuel rod in terms of curvature range/amplitude can be risky. This is because the response of rods is generally not symmetric with respect to the curvature origin. The sign and magnitude of mean curvature depend on the as-received condition of a rod specimen and on loading conditions as well. However, the observation raised a concern because the use of curvature range/amplitude did not reflect the real maximum stress level of outer fiber in a bending rod. An alternate approach is based on the maximum of absolute curvature extremes, $|\kappa|_{MAX}$, as defined by the following:

$$|k|_{max} = \max(|k_{max}|, |k_{min}|) . \tag{6}$$

For a given specimen, the $|\kappa|_{max}$ given by Eq. (6) corresponds to the curvature that causes the maximum stress levels. Curvatures as a function of number of cycles are shown in Fig. 5 represented by the curvature amplitude and the maximum of absolute curvature extremes. The results indicate that the curve of curvature versus number of cycles could be raised to a certain degree if the maxima were used instead of amplitude. The factor of power function was increased by 23%.

k-N Curve and Effect of Hydrogen Contents

There was no specific hydrogen content data available for the tested HBR rod segments. However, the ranges of hydrogen content on the parent fuel rods were available, and the hydrogen contents of the tested rod segments can be estimated based on where they were taken from. The estimated hydrogen contents of the HBR rods ranged from 360 to 750 ppm. An assembly of cycle tests is presented in Fig. 6. It can be clearly seen that the curve of curvature amplitude vs. the number of cycles was shifted down and to the left when hydrogen content was equal to or greater than 700 ppm. Under the same curvature range, the fatigue life of the specimens with higher hydrogen content is shorter than the fatigue life of specimens with lower hydrogen content.
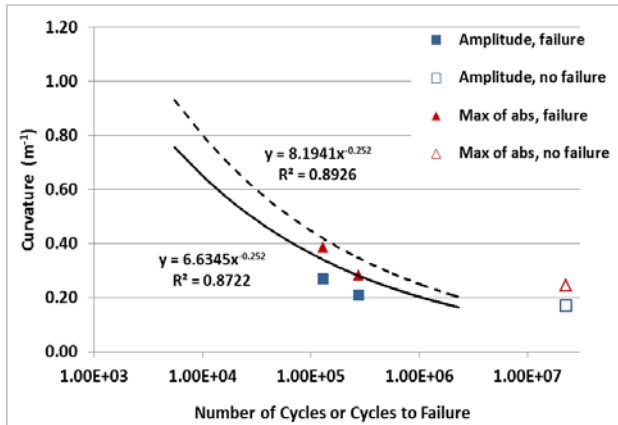

Fig. 5. Maxima of absolute (abs) curvature extremes and curvature amplitudes as a function of number of cycles. Solid markers represent tests with specimen failures; open markers indicate tests without failures. The power function was obtained from curve fitting based on the HBR data set [7]; solid line corresponds to amplitudes, and dash line corresponds to maxima of absolute.
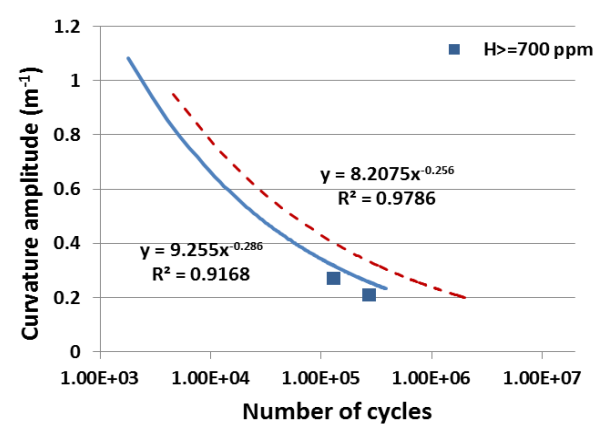
Fig. 6. Curvature amplitudes as a function of number of cycles or k-N curve for HBR SNF with various levels of hydrogen content. The power function was obtained from curve fitting based on the HBR data set; the solid line corresponds to H >= 700ppm, and the dashed line corresponds to H < 700pm [7].

6

Static Response of SNF

Fig. 7 summarizes the equivalent stress and strain results from static bending testing on SNF rods (HBR, NA M5^{TM}, and MOX M5^{TM}). The static responses of NA M5^{TM} and MOX M5^{TM} specimens were quite consistent. Three stages can be identified in trend curve (Fig. 7) with the first and second deflection points (approximately 90 and 300 MPa, respectively). The curves of NA and MOX fuels were obviously well below those of HBR fuels. The maximum stress of HBR fuels at the same relative displacement (24.00 mm) was between 733 and 748 MPa, while those of NA and MOX were between 510 and 530 MPa. The maximum strains among the three tested fuels were close in value, ranging from 1.67 to 1.98%. The stress level at the first deflection for NA/MOX M5^{TM} fuels was located near 100 MPa, and the second was between 300 and 400 MPa. These stress levels are lower than those of the HBR fuel [7].

A comparison revealed a large discrepancy between the curves of CIRFT static results and the Pacific Northwest National Laboratory (PNNL) data for Zircaloy-4 cladding, at fast neutron fluence of 12 10^{25} n/m^2. A preliminary investigation showed that the reduction of pellet moment inertia by 50% could actually bring the CIRFT curve up enough to close the gap, i.e., $I = I_c + 0.5*I_p$. The same procedure was applied to processing NA and MOX fuel data; the results are given in Fig. 8. The use of reduced inertia of pellet in the calculation of equivalent stress raised the stress as expected. For example, the maximum attained levels are between 700 and 725 MPa. It is emphasized that the concept of reduced pellet moment of inertia and the use of Eqs. (2) and (3) were implemented to demonstrate the relative stress levels between different SNFs. More FEA modelling effort is needed to understand the deformation mechanisms and to predict the response of the SNF rod under the corresponding loading condition.
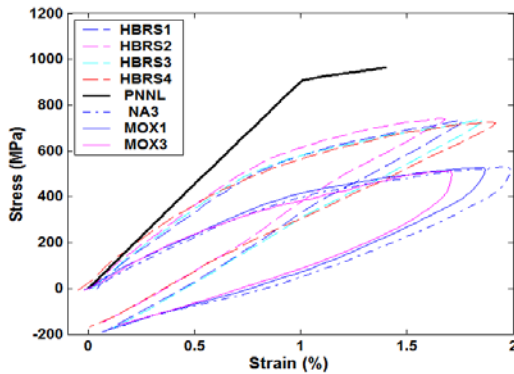

Fig. 7. Stress-strain curves based on static testing results for HBR, NA, and MOX SNF. Relative displacement was 24.00 mm; the loading/unloading rate at each point was 0.1/0.2 mm/s.
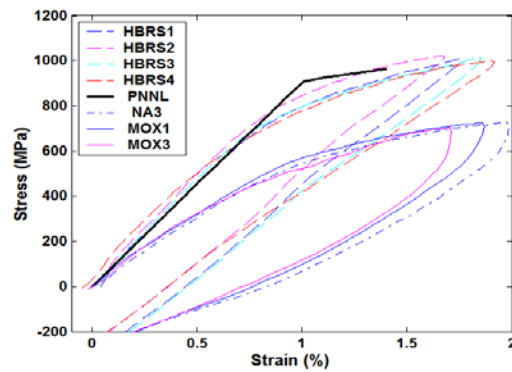
Fig. 8. Stress-strain curves based on static testing results for HBR, NA, and MOX SNF. The equivalent stress is based on Eq. (2) with $I = I_c + 0.5*I_p$.

DISCUSSION OF FINITE ELEMENT ANALYSES RESULTS

Based on FEA simulation results of 6.25 N-m load and further verification from HBU HBR rod bending test results, the localized system (stress-curvature) biases and uncertainties associated with CIRFT global response on the SNF rod system performance can be quantified and summarized as discussed below [4, 11–12]. The details of FEM models are shown in Fig. 9.

Initially, with perfect interface bonding and without fuel pellet and clad fracturing, the pellets in the HBR rod will carry more bending moment resistance than the clad under NCT vibration. The maximum stress resides in the pellets, and the stresses at the clad and pellet are both below the yield condition. Therefore, the system is in a linear elastic state under the target bending loads. Upon fuel pellet failure, including debonding at the pellet-pellet interfaces, the load carrying capacity shifts from the fuel pellets to the clad under clad tension cycle. The clad starts to carry most of the bending moment at the pellet-pellet interface

region, resulting in localized stress concentrations in the clad. However, under the 6.25 N-m bending moment, the clad does not yield. With good cohesion bonding at the pellet-clad interfaces, the pellets can continue to support the clad and carry a sufficient portion of the bending moment resistance; therefore, most of the clad at the gauge section remains in the linear elastic range. A shear stress surge occurs inside the cladding at the pellet-pellet interface regions.

When further debonding occurs at the pellet-clad interfaces, the embedded pellets can no longer provide effective structural support to the clad; nor can they assist load transfer within the HBR rod system. Thus most of the load-carrying capacity shifts to the clad throughout the entire gauge section. The shift leads to high stress concentrations in the clad throughout entire gauge section instead of at localized pellet-pellet interface regions. At this point, the impact of the property change in the interface material is very limited. The clad does not yield because of the high material yield strength and the low bending load of 6.25 N-m. There is no resulting shear stress concentration inside the clad for interface debonding.
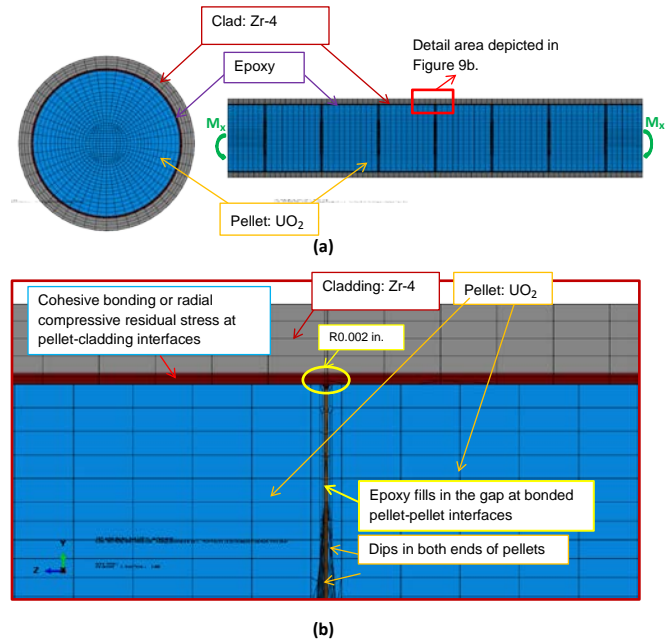

Fig. 9 Details of FEA models.

When the pellets contact and ping against each other, they seem to take over a significant portion of the bending load resistance, especially where there are no gaps at the pellet-pellet interfaces. This pellet pinning action clearly mitigates and avoids stress concentration and the potential yielding at the compression side of the clad. The simulation cases are summarized in Table 1. The main parameter flexural rigidity, *EI,* is compared case by case. The flexural rigidity increases by up to 26% for the pellet-pellet interface debonding with gaps. The immediate consequence of interface debonding is a shift in the load-carrying capacity from the fuel to the clad, as well as a reduction in flexural rigidity. For example, the flexural rigidity is 77 $N \cdot m^2$ when the pellets are perfectly bonded with epoxy. In the case with gaps at the pellet-pellet interfaces, when there is debonding at the pellet-pellet interfaces alone, the flexural rigidity drops by 49% to 39 $N \cdot m^2$. In the case without gaps, it drops by 31%, to 53 $N \cdot m^2$. Further debonding at the pellet-clad interfaces causes the flexural rigidity to drop further, by 26% with gaps and 19% without gaps. Overall, for cases with and without gaps, flexural rigidity drops by about 62% and 44%, respectively, between the perfect bond and the debond cases at all interfaces. The changes in flexural rigidity are similar for different bonding conditions for the two types of interfacial material.

Flexural rigidity is reduced more by debonding at pellet-pellet interfaces than by debonding at pellet-clad interfaces. Table 1 shows a flexural rigidity that is about 30% higher for the fuel rod without gaps, indicating a significant increase in system stiffness over the case with gaps. Therefore, the gaps at the interfaces of the fuel rod system have a significant impact on system reliability, especially at pellet-pellet interfaces. The flexural rigidity and bending moment resistance capacity of the fuel rod are highly dependent on interface bonding efficiency at pellet-clad and pellet-pellet interfaces. This discovery was validated by ORNL reversal bending fatigue test results performed on the fuel rod with HBR pellet inserts. The estimates for curvature and the associated flexural rigidity vary widely between three deflection data points chosen from a relatively global area and a local area. Because of a lack of pellet support at the debonded interface, the local tensile clad curvature is ~3 to 4 times that of the global curvature at the tension side of the clad. At the compression side of the clad, the curvature and flexural

rigidity estimated from the deflection data in the global two inch gauge section range are the same. However, the curvature estimated in a localized area from the compression side is ~ ⅓ to ½ that estimated from the tension side. With pellet-pellet debonding at the clad's compressive stress region, pellet-pellet pinning continues to provide good support to resist flexural deformation. Locally, the flexural rigidity estimated from the local compression side is double or triple that estimated from the local tension side.

Table I. The Flexural Rigidity Comparison between the Different Bonding and Debonding Cases

Interface Bonding Conditions	Flexural Rigidity EI (N·m^2)	Reduction from Perfect Bond (%)	Reduction from Only Pellet-Pellet Debond to Further Pellet-Clad Debond (%)	Increase from with gaps to without gaps (%)
Perfect bond with epoxy	77			
Pellet-pellet interface with gap debond, pellet-clad interface bonded with epoxy	39	49		
Pellet-pellet interface without gap debond, pellet-clad interface bonded with epoxy	53	31		26
Pellet-pellet interface with gap debond, pellet-clad interface debonded with epoxy	29	62	26	
Pellet-pellet interface without gap debond, pellet-clad interface debonded with epoxy	43	44	19	33

The clad stress investigation reveals that the fuel rod system neutral axis shifts with interfacial debonding. The stress estimation based on induced curvature and flexural strain adjusted by the neutral axis shifting shows fairly realistic results. The comparison between clad stress at the pellet-pellet interface region and away from the interface region shows a nonuniform stress distribution. The normal change in clad stress for different interface bonding conditions, especially a change in axial stress σ_{zz}, reveals a similar trend in the change in curvature. σ_{yz} dominates in the shear stress results. For the case without gaps at pellet-pellet interfaces, the σ_{yz} at the compression side is much smaller than that at the tension side as a result of pellet-pellet pinching.

Fractography
PIE study was performed by using an optical microscope in an ORNL hot cell on the fractured/failed CIRFT specimens [4, 7]. The failed specimens were tested under pure dynamic loading. Almost all the CIRFT tests were failed at the pellet-pellet interface. The

Fig. 10 (a) Lateral or front view, (b) transverse view, of fracture surface for NA2 specimen tested under ±10.16 N·m 5Hz, $N_f = 2.20 \times 10^4$ cycles.

typical fracture surfaces for these specimens are presented in Fig. 10, which shows that the interface failure mode prevails or dominates in SNF fatigue tests, and the fuel-pellet interface seems to remain intact. The maximum clad stress sites show clad delamination occurred before final spontaneous fracture taking place.

CONCLUSIONS
The CIRFT tests were conducted on HBU SNF fuels of Zr-4 and M5^{TM} cladding. Almost all the tested SNF rods failed at pellet-pellet interface regions. Data analysis demonstrated that it is necessary to
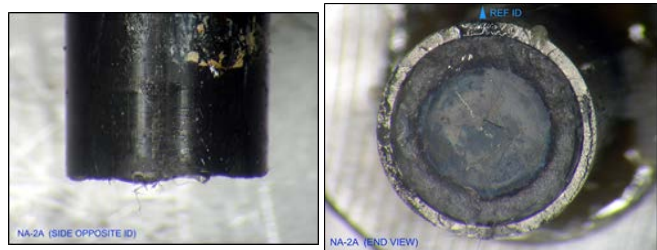
characterize the fatigue life of SNF rods in terms of both the curvature amplitude and the maximum of absolute curvature extremes. The latter is significant because the maxima of extremes signify the maximum of tensile stress of the outer fiber of the bending rod. The load amplitude has been the dominant factor that controls the fatigue life of rods, but the hydrogen content also has an important effect on the SNF fatigue life. Based on a series of FEA simulations, the impact of the interface bonding characteristics on SNF vibration integrity, the distribution of moment carrying capacity between pellets and clad, and the impact of the interface material on the flexural rigidity of the fuel rod system are all important factors to be considered when evaluating the clad/fuel system under NCT.

Sensor benchmark protocol development will be continued to refine the CIRFT global strain measurement. The BWR SNF rods that may have different vibration characteristics compared to PWR SNF rods will be investigated in the near future.

REFERENCES

1. E. J. RUZAUSKAS, and K. N. FARDELL, "Design, Operation, and Performance Data for High Burnup PWR Fuel from H. B. Robinson Plant for Use in the NRC Experimental Program at Argonne National Laboratory," Electric Power Research Institute, EPRI Report 1001558, 2001.
2. B. HANSON, H. ALSAED, C. STOCKMAN, D. ENOS, R. MEYER, and K. SORENSON, "Gap Analysis to Support Extended Storage of Used Nuclear Fuel," Rev. 0, U.S. Department of Energy Used Fuel Disposition Campaign, January 31, 2012.
3. H. WANG, J.-A. J. WANG et al., "Development of U-frame Bending System for Studying the Vibration Integrity of Spent Nuclear Fuel," *Journal of Nuclear Materials* 440, 201–13 (2013).
4. J-A. WANG, H. WANG, H. JIANG, B. BEVARD, R. HOWARD, "CIRFT Testing Results on High Burnup UNF," *M2-FCRD-UFD-2014-000053*, September 2014.
5. J.-A. WANG, H. WANG, B. BEVARD, M. FLANAGAN, et al., "Surrogate SNF Vibration Integrity Investigation," *2014 ANS Meeting*, June 15-19, 2014, Reno Nevada.
6. J.-A. J. WANG, H. WANG, et al., "Reversible Bending Fatigue Test System for Investigating Vibration Integrity of SNF During Transportation," *PATRAM 2013*, San Francisco, Calif., August 18–23, 2013.
7. J.-A. J. WANG and H. WANG, "Mechanical Fatigue Testing of High-Burnup Fuel for Transportation Applications," NUREG/CR, ORNL/TM-2014/214, Oak Ridge National Laboratory, December 2014.
8. J-A. WANG, H. WANG, B. BEVARD, "Reversible Bending Fatigue Testing on Zry-4 Surrogate Rods," *WM2014 Conference*, Phoenix, AZ, March 02-06, 2014.
9. J.-A. J. WANG et al., "SNF Test System for Bending Stiffness and Vibration Integrity," *International High-Level Radioactive Waste Management Conference*, Albuquerque, N.M., April 28–May 2, 2013.
10. J.-A. WANG, H. WANG, et al., "The Development of Reversible Bending Fatigue Tester and Its Application to High Burnup SNF Vibration Integrity Investigation under Normal Transportation," ORNL/TM-2013/573.
11. H. JIANG, J-A WANG, and H. WANG, "Potential Impact of Interfacial Bonding Efficiency on SNF Vibration Integrity during Normal Transportation," *ASME PVP Conference*, July 20-24, 2014, Anaheim CA.
12. J-A. WANG, H. WANG, and H. JIANG, "Using Finite Model Analysis and Out of Hot Cell Surrogate Rod Testing to Analyze High Burnup SNF Mechanical Properties," *FCRD-UFD-2014-000603,* August 2014.

ACKNOWLEDGEMENTS